

Solving nonequilibrium statistical mechanics by evolving autoregressive neural networks

Ying Tang,^{1,*} Jing Liu,^{2,*} Jiang Zhang,^{2,3} and Pan Zhang^{4,5,6,†}

¹*International Academic Center of Complex Systems,
Beijing Normal University, Zhuhai 519087, China*

²*School of Systems Science, Beijing Normal University, Beijing 100875, China*

³*Swarma Research, Beijing 102308, China*

⁴*CAS Key Laboratory for Theoretical Physics, Institute of Theoretical Physics,
Chinese Academy of Sciences, Beijing 100190, China*

⁵*School of Fundamental Physics and Mathematical Sciences,*

Hangzhou Institute for Advanced Study, UCAS, Hangzhou 310024, China

⁶*International Centre for Theoretical Physics Asia-Pacific, Beijing/Hangzhou, China*

(Dated: August 18, 2022)

Nonequilibrium statistical mechanics inherits the challenges of the equilibrium, including accurately describing the joint distribution of a large number of variables. It also poses new challenges as the joint distribution evolves over time. While a number of methods have been proposed, e.g., tensor networks for one-dimensional lattices, we lack a method for arbitrary finite time in higher dimensions. In this work, we propose a general approach to study the time evolution of nonequilibrium systems in statistical mechanics by autoregressive neural networks. Specifically, our method offers direct sampling and efficient computation of the normalized probabilities and dynamical partition functions, uncovering the dynamical phase transition over time. We apply the method to a prototype model of nonequilibrium statistical mechanics, the kinetically constrained models of structural glasses up to three dimensions. The obtained results reveal the phase diagram of the time and counting field, as well as the scaling relations. Our approach paves the way toward solving nonequilibrium statistical mechanics using tools in modern machine learning.

Introduction.— Tracking time evolution, computing the dynamical partition function, and characterizing the emergence of the dynamical phase transition are crucial tasks in nonequilibrium statistical mechanics [1–3]. For example, a first-order dynamical phase transition between active and inactive phases in space and time [4] was found in kinetically constrained models (KCM) [5], giving insights to the dynamical heterogeneity of the glass transition [6]. However, studying the finite-time evolution of nonequilibrium systems is challenging, because it requires estimating the whole spectrum of the dynamical generator rather than computing only the largest eigenvalue in the long-time limit [7–18] based on the large deviation theory [19–22]. Analytically, it is intractable except for rare cases [23–27]; numerically, the main difficulty of studying the time evolution arises from expressing the high-dimensional probability distribution with a growing complexity when the correlation builds up at each time step.

In this work, we propose to study the time evolution of nonequilibrium systems with general topology at arbitrary finite time by variational autoregressive networks (VAN), which offer an ideal model for describing the joint distribution of configurations. Autoregressive networks have been previously utilized to study equilibrium statistical mechanics [28–31] and quantum many-body systems [32–39]. Here, we adapt it to an evolving probability distribution in order to study the time evolution of nonequilibrium dynamics. Our approach provides the ability to directly sample configurations and compute the dynami-

cal partition function at arbitrary finite time. This leads to an efficient method to estimate statistics of dynamical observables and uncover the dynamical phase transitions. We apply it to KCM for glassy dynamics, including the Fredrickson-Andersen (FA) model [40] and variants of the East model [4, 12, 41], in one dimension (1D), two dimensions (2D), and three dimensions (3D).

For the 1D finite-time problem, our method gives results that are consistent with the existing results of matrix product states [42]. For the 2D and 3D cases, our method uncovers dynamical phase transitions and critical exponents of the finite-time scaling. For the high-activity sector under the negative counting field, we observe the emergence of the high-activity characteristic spatial structures of 2D KCMs. We also discuss that the proposed neural-network method can be applied to nonequilibrium systems with other types of dynamics and other interactive topologies in a straightforward way.

Time evolution in nonequilibrium systems.— The stochastic Markov dynamics evolving continuously in time can be described by a master equation. We consider a system of size N and M configurations ($M = 2^N$ for spin systems), with each configuration $|\mathbf{x}\rangle \equiv \{x_1, x_2, \dots, x_N\}$. The probability of the system at time t is described by the probability vector $|P_t\rangle = \sum_{\mathbf{x}} P_t(\mathbf{x})|\mathbf{x}\rangle$. It evolves under the stochastic master equation [43]:

$$\frac{d}{dt}|P_t\rangle = \mathbb{W}|P_t\rangle, \quad (1)$$

with generator $\mathbb{W} = \sum_{\mathbf{x}' \neq \mathbf{x}} w_{\mathbf{x}, \mathbf{x}'} |\mathbf{x}'\rangle\langle \mathbf{x}| - r_{\mathbf{x}} |\mathbf{x}\rangle\langle \mathbf{x}|$. Here, $w_{\mathbf{x}, \mathbf{x}'}$ is the transition rate from the configuration $|\mathbf{x}\rangle$ to $|\mathbf{x}'\rangle$, and $r_{\mathbf{x}} = \sum_{\mathbf{x}' \neq \mathbf{x}} w_{\mathbf{x}, \mathbf{x}'}$ is the escape rate from $|\mathbf{x}\rangle$.

From a macroscopic point of view, a typical quantity we are interested in is the time-extensive dynamical observable $\hat{K} = \sum_{i=0}^{I-1} \alpha(\mathbf{x}_{t_i}, \mathbf{x}_{t_{i+1}})$, which is incremented along a trajectory $\omega_t = \{\mathbf{x}_0 \rightarrow \mathbf{x}_{t_1} \rightarrow \dots \rightarrow \mathbf{x}_{t_I}\}$ in the time window $[0, t]$ with $t = t_I$. The stepwise increment α depends on the configuration transitions [44]. The probability of observing the dynamical observable with a value K is obtained by summing over all possible trajectories: $P_t(K) = \sum_{\omega_t} p(\omega_t) \delta[\hat{K}(\omega_t) - K]$, where $p(\omega_t)$ is the probability of trajectory ω_t . In this work, we focus on a characteristic dynamical observable, the dynamical activity, measuring the number of configuration changes (e.g., spin flips) with $\alpha(\mathbf{x}_{t_i}, \mathbf{x}_{t_{i+1}}) = 1$ [4, 45]. The corresponding “tilted” generator [44] is defined as

$$\mathbb{W}_s = \sum_{\mathbf{x}' \neq \mathbf{x}} e^{-s} w_{\mathbf{x}, \mathbf{x}'} |\mathbf{x}'\rangle\langle \mathbf{x}| - r_{\mathbf{x}} |\mathbf{x}\rangle\langle \mathbf{x}|. \quad (2)$$

For the dynamical observable \hat{K} with the counting field s , the dynamical partition function is defined as the moment generating function $Z_t(s) = \sum_K P_t(K) e^{-sK} = \sum_{\omega_t} p(\omega_t) e^{-s\hat{K}(\omega_t)}$. It plays a central role in nonequilibrium statistical systems [46] since it stores all the statistics of the dynamical observable. Additionally, it can be evaluated as a tilted generator $e^{t\mathbb{W}_s}$ [4, 7]:

$$Z_t(s) = \langle -|e^{t\mathbb{W}_s}|ss \rangle, \quad (3)$$

where $|ss\rangle$ is the steady state probability vector under \mathbb{W} , and $\langle - | = \sum_{\mathbf{x}} \langle \mathbf{x} |$ is the “flat” state. The moments, such as the average dynamical activity per unit of time and site, can be calculated as $k_t(s) = -\frac{1}{Nt} \frac{d}{ds} \ln Z_t(s)$.

Tracking time evolution using autoregressive neural networks.— A natural approach to study nonequilibrium statistical mechanics is tracking $|P_t\rangle$ in the evolution equation, Eq. (1). Unfortunately, the exact representation of $|P_t\rangle$ requires a computational effort that is exponential in the number of variables. Hence we need an efficient method to approximately represent $|P_t\rangle$. Here, we consider a specific neural network model, the autoregressive neural network [30, 31], as a variational ansatz for the time-evolved distribution $|P_t\rangle$ in Eq. (1). In autoregressive neural networks, the joint probability distribution $|P_t\rangle$ is represented using the product of conditional probabilities, which are further parameterized using a neural network. The advantage of using the autoregressive network is that since all the conditional probabilities are stored, one can efficiently generate unbiased samples associated with normalized probabilities. The samples and probabilities can be used to compute quantities such as energy and entropy, and construct loss functions to update the parameters of $|P_t\rangle$.

Based on the autoregressive representation of $|P_t\rangle$, we evaluate Eq. (3) by applying the operator $e^{\delta t\mathbb{W}_s}$ se-

quentially as $Z_t(s) \approx \langle -|(\mathbb{T}_s)^I|ss \rangle$ (Suzuki-Trotter decomposition [47]), where the transition operator $\mathbb{T}_s = (\mathbb{I} + \delta t\mathbb{W}_s) \approx e^{\delta t\mathbb{W}_s}$, \mathbb{I} denotes the identity operator, and $t = I\delta t$. Without loss of generality, we consider the one-step evolution from a normalized probability vector $|\hat{P}_i^{\theta_i}\rangle$ at time i with parameters θ_i . We use the autoregressive neural network as a normalized variational probability vector $|\hat{P}_{i+1}^{\theta_{i+1}}\rangle$ at time $i+1$ to approximate the normalized state $|\hat{Q}_i^{\theta_i}\rangle = \mathbb{T}_s |\hat{P}_i^{\theta_i}\rangle / Z_{i+1}(s)$ by minimizing the Kullback-Leibler (KL)-divergence between the two distributions,

$$D_{KL}[\hat{P}_{i+1}^{\theta_{i+1}} || \hat{Q}_i^{\theta_i}] = \mathcal{L}_{i+1} + \ln Z_{i+1}(s), \quad (4)$$

where

$$\mathcal{L}_{i+1} = \sum_{\mathbf{x}} \hat{P}_{i+1}^{\theta_{i+1}}(\mathbf{x}, s) \left[\ln \hat{P}_{i+1}^{\theta_{i+1}}(\mathbf{x}, s) - \ln \mathbb{T}_s \hat{P}_i^{\theta_i}(\mathbf{x}, s) \right]. \quad (5)$$

Minimizing the KL-divergence is equivalent to minimizing \mathcal{L}_{i+1} , which plays a role analogous to the variational free energy in equilibrium statistical mechanics. Since the autoregressive network supports unbiased sampling in parallel to compute \mathcal{L}_{i+1} , we estimate the gradients with respect to parameters θ_{i+1} by the REINFORCE algorithm [48]:

$$\nabla_{\theta_{i+1}} \mathcal{L}_{i+1} = \sum_{\mathbf{x}} \hat{P}_{i+1}^{\theta_{i+1}}(\mathbf{x}, s) \left\{ \nabla_{\theta_{i+1}} \ln \hat{P}_{i+1}^{\theta_{i+1}}(\mathbf{x}, s) \right. \\ \left. \cdot \left[\ln \hat{P}_{i+1}^{\theta_{i+1}}(\mathbf{x}, s) - \ln \mathbb{T}_s \hat{P}_i^{\theta_i}(\mathbf{x}, s) \right] \right\}, \quad (6)$$

where the summation is over all samples generated using the autoregressive network.

As an essential outcome of the algorithm, the dynamical partition function can be computed as a product of the normalization constants at each time step $Z_t(s) \approx \prod_{i=1}^I Z_i(s)$. For each normalization constant, the non-negativity of the KL-divergence ensures that Eq. (5) provides a lower bound for the estimation of $\ln Z_{i+1}(s)$, with

$$\ln Z_{i+1}(s) \geq -\mathcal{L}_{i+1}. \quad (7)$$

The equality holds when the autoregressive network faithfully learns the evolved distribution and achieves zero KL-divergence.

The advantages of the autoregressive network model over the existing tensor network model in representing $|P_t\rangle$ mainly come from its generality. The neural network ansatz can be used in systems with various topologies, in contrast to the matrix product states that were designed for a one-dimensional system. On the one hand, the VAN representation of $|P_t\rangle$ works for systems with arbitrary topology without modifying the structure of autoregressive network [30]; on the other hand, we can design the architecture of autoregressive networks to fit the topology of the system. For example, for 2D systems, we can use convolutional networks, as in image recognition [50, 51];

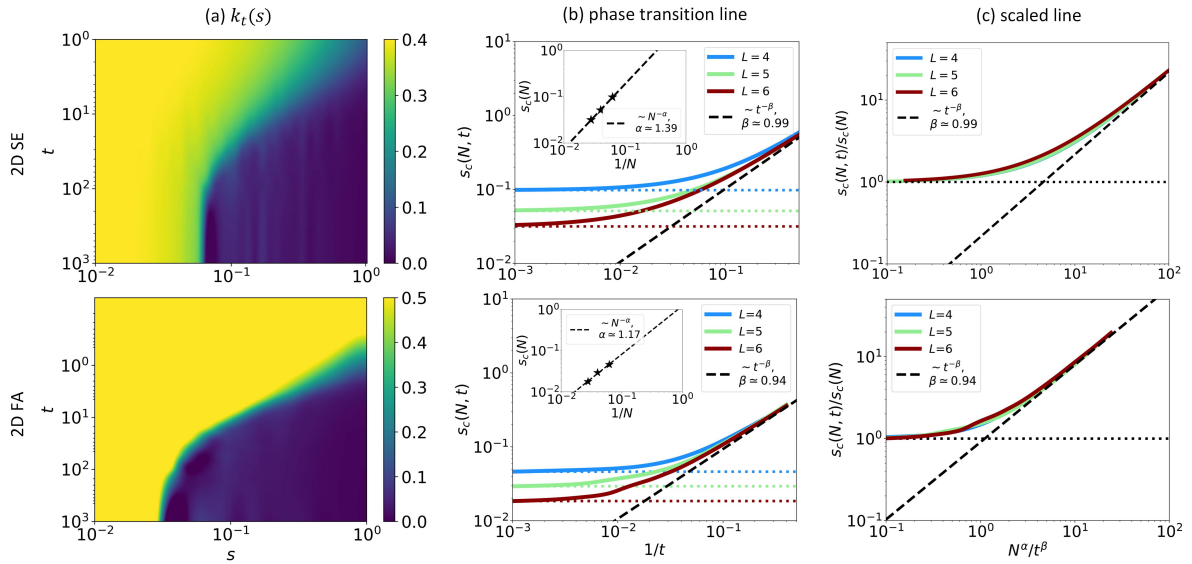


FIG. 1. (Color online) Characterization of the dynamical phase transition over time. The top panel is the 2D SE model, and the bottom panel is the 2D FA. (a) The dynamical activity $k_t(s)$ over time t reveals the phase transition versus the counting field s , with $L = 5$. The color denotes the dynamical activity. (b) The critical point $s_c(N, t)$ over time, giving critical exponents α from $s_c(N) \sim N^{-\alpha}$ at the steady state (the horizontal dotted lines and the inset) and β from the finite-time scaling $t^{-\beta}$ (the black dashed line). (c) The scaled phase transition lines, with $s_c(N, t)/s_c(N)$ and time scaled as $N^\alpha t^{-\beta}$, are collapsed together. Parameters: $c = 0.5$, $L = 4, 5, 6$. See Supplemental Material [49] for the results for the 3D SEF model.

for 3D systems, we can leverage 3D convolutions; and for sparse networks, graph neural networks [52, 53] have been shown to be efficient in the machine learning community.

Application to the kinetically constrained models.—

The proposed approach is applicable to a wide class of nonequilibrium systems in statistical mechanics when their evolution contains a countable number of state transitions. A representative class is KCMs [4], whose number of state transitions (spin flips) for each configuration equals the system size N . We focus on two paradigmatic KCMs, namely, FA [40] and variants of East [41] models, on a lattice of size $N = L$ in 1D, $N = L^2$ in 2D, and $N = L^3$ in 3D, with binary spins $n_j = 0, 1$ for $j = 1, \dots, N$ and 2^N configurations in total. We remark that the finite-time properties (e.g., the dynamical partition function $\ln Z_t(s)$) of KCMs on lattices with dimension greater than one have not been achieved before.

The Markovian generators are written as

$$\mathbb{W} = \sum_{i=1}^N f_i [c\sigma_i^+ + (1-c)\sigma_i^- - c(1-n_i) - (1-c)n_i], \quad (8)$$

where σ_i^\pm are the Pauli raising and lowering operators flipping site i up and down, and $c \in (0, 0.5]$ controls the rates of flipping up. The FA model has f_i as the number of nearest-neighbor up spins, the 1D East model has f_i as the number of left nearest-neighbor up spins, the 2D South-East (SE) has the left and above, and the 3D South-East-Front (SEF) has the left, above and back.

The generator acts on each configuration and contributes to the case with only one spin flip between two configurations. Starting from the steady state of the non-tilted generator \mathbb{W} , the evolution of the system can be tracked when the operator matrix is sparse. For example, each configuration only has N connected configurations to transit in or out for KCMs; that is, the probability at each time is updated using only their neighbors' probabilities of batch samples.

We consider open boundary conditions for the convenience of comparing results with the literature. The boundary sites are up for 1D [42] and down for 2D [15] and 3D. For the 2D FA model, the configuration with all down spins is excluded to avoid this disconnected configuration. To access the largest ergodic element in the configuration space, the first spin is fixed up for 2D and 3D East variants. Note that all figures of configurations do not include boundary sites.

Active-inactive transition for 2D and 3D KCMs—
At the steady state, the FA and East models display an active-inactive dynamical phase transition [4, 11, 13, 54] between two dynamical phases with extensive or subextensive activities with $s > 0$. For finite-time dynamics, the transition point has not been explored except for 1D [42]. For 1D systems, we have checked that the dynamical partition function computed using our method coincides well with the exact values, and the long-time limit of our results matches with the steady-state SCGF from the variational Monte-Carlo method [15] (Supplemental

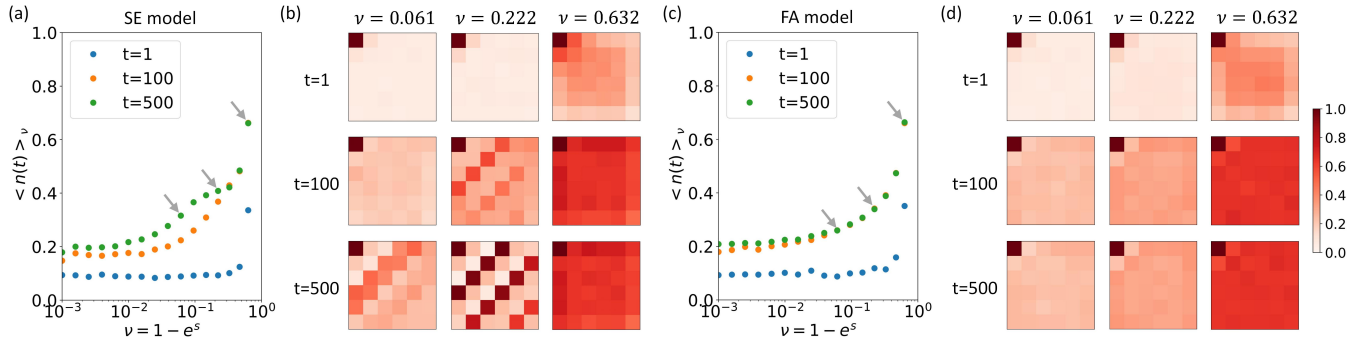


FIG. 2. (Color online) The emergence of the active phases. The 2D SE (a, b) and 2D FA (c, d) models with $c = 0.05$, $L = 6$ and $s < 0$. (a, c) The average density in the active phase at various time points for $c = 0.05$. The grey arrows point to the chosen ν (introduced for $s < 0$) for showing the average spatial configurations in (b,d). (b, d) Time evolution of spatial configurations at various time points (rows) for different ν values (columns). For the comparison between the two models, the left-up corner spin of both models is fixed up. The color denotes the averaged up spins, with the same color bar in (d).

Material [49]). These results are also consistent with the previous [42] by tensor networks on 1D [49].

The autoregressive network allows us to represent the time-dependent probability distribution for systems with arbitrary topology, hence enabling us to investigate finite-time properties KCMs on 1D, 2D, and 3D lattices in a unified way. We conduct a scaling analysis of the critical point as a function of system size and time, with scanning lattice sizes $L = 4, 5, 6$ for 2D and $L = 2, 3, 4$ for 3D. When time evolves, the finite-size effects motivate to approximate $s_c(N, t) \approx s_c(N) + s_c(t)$. The scaling of system size $s_c(N) \sim N^{-\alpha}$ is obtained from the long-time limit, giving the exponent $\alpha \gtrsim 1$ for 2D (Fig. 1b) and 3D (Supplemental Material [49]). We further estimate the scaling of time by fitting $\ln[s_c(N, t) - s_c(N)]$ versus $-\ln(t)$, giving $s_c(t) \sim t^{-\beta}$ with $\beta \approx 1$ for 2D and 3D, which has not been revealed before. We then scale $s_c(N, t)$ by $s_c(N)$ and time as $N^\alpha t^{-\beta}$ and find that $s_c(N, t)$ curves can be collapsed together (Fig. 1c).

Active phases for 2D models— The steady-state properties have been investigated for 2D SE and FA models in the literature [15]. It has been found that with high activity ($s < 0$) and $c < 0.1$, the average density (versus $\nu \equiv 1 - e^s$) of the two models has a distinct behavior: it displays a plateau phenomenon for the 2D SE model, which is absent in the 2D FA model. We go beyond the steady state and study the time evolution of the average density of up spins $\langle n(t) \rangle_\nu$ and the emergence of characteristic spatial structures over time (Fig. 2). With a small $c = 0.05$, we discover that the 2D SE model has density plateaus, which are absent in the 2D FA model. For average spatial configurations, the 2D SE model forms structures with up-spin diagonal bands separated by down-spin bands, and the number of bands varies over ν . The 2D FA model does not have such characteristic bands, even when its first spin is also fixed up.

We observe that the accumulation of the error mainly occurs when the dynamics of the system change dra-

matically over time, e.g., when the active-inactive phase transition occurs. Identifying these time points by trial and error helps find the most efficient way of increasing epochs for accuracy at certain time points. An alternative way of resolving the issue is to project the evolution into two parts: one follows the largest eigenvalue of the tilted generator, i.e., the SCGF calculated from the steady state, and the other follows from a modified tilted generator (Supplemental Material [49]). When the modified generator reaches a steady value, one can stop the simulation and extrapolate it by using the SCGF. Besides, capturing the active-inactive transition requires efficient sampling of rare inactive configurations with few up spins, which is accessible by importance sampling [49].

Conclusions.— We have presented a general framework to study the dynamics of nonequilibrium statistical systems based on neural networks. Given the microscopic transitions between the connected configurations, our method captures the dynamics over time by counting all the allowable transitions to the connected configurations of the sampled configurations. Using extensive numerical experiments, we have demonstrated that our approach uncovers the dynamical phase transition over time and scaling relations in the KCMs on 2D and 3D lattices. Our results also reveal the emergence of characteristic spatial structures of the active phases. The method can be applied to general nonequilibrium systems with arbitrary interactive topologies, such as the Fredkin model generalized to the 2D honeycomb lattice [55] and epidemic spreading on graphs [56]. A possible architecture of autoregressive models could be the graph neural networks [52, 53] adapted to the specific topologies. Another direction is to use the VAN for sampling rare trajectories [57] in high-dimensional lattice systems, with the help of the Doob operator [18].

A pytorch implementation of our algorithm will be available upon the acceptance of the manuscript. We thank Online Club Nanothermodynamica for discussions,

and Luke Causer and Corneel Casert for the helpful communication. This work is supported by Project 11747601, 11975294, 12105014 of National Natural Science Foundation of China. P.Z. is also supported by the Key Research Program of Frontier Sciences, CAS Grant No. QYZDB-SSW-SYS032. The HPC is supported by Dawning Information Industry Corporation Ltd and Interdisciplinary Intelligence SuperComputer Center of Beijing Normal University, Zhuhai.

* These authors contributed equally

† Corresponding author: panzhang@itp.ac.cn

- [1] M. Esposito, U. Harbola, and S. Mukamel, Nonequilibrium fluctuations, fluctuation theorems, and counting statistics in quantum systems, *Rev. Mod. Phys.* **81**, 1665 (2009).
- [2] T. Chou, K. Mallick, and R. K. Zia, Non-equilibrium statistical mechanics: from a paradigmatic model to biological transport, *Rep. Prog. Phys.* **74**, 116601 (2011).
- [3] *Nonequilibrium Statistical Physics of Small Systems: Fluctuation Relations and Beyond*, edited by R. Klages, W. Just, and C. Jarzynski (Wiley-VCH, New York, 2013).
- [4] J. P. Garrahan, R. L. Jack, V. Lecomte, E. Pitard, K. van Duijvendijk, and F. van Wijland, Dynamical first-order phase transition in kinetically constrained models of glasses, *Phys. Rev. Lett.* **98**, 195702 (2007).
- [5] F. Ritort and P. Sollich, Glassy dynamics of kinetically constrained models, *Adv. Phys.* **52**, 219 (2003).
- [6] J. P. Garrahan and D. Chandler, Geometrical explanation and scaling of dynamical heterogeneities in glass forming systems, *Phys. Rev. Lett.* **89**, 035704 (2002).
- [7] V. Lecomte and J. Tailleur, A numerical approach to large deviations in continuous time, *J. Stat. Mech.* **2007**, P03004 (2007).
- [8] T. Nemoto, F. Bouchet, R. L. Jack, and V. Lecomte, Population-dynamics method with a multicanonical feedback control, *Phys. Rev. E* **93**, 062123 (2016).
- [9] U. Ray, G. K.-L. Chan, and D. T. Limmer, Importance sampling large deviations in nonequilibrium steady states. i, *J. Chem. Phys.* **148**, 124120 (2018).
- [10] D. Jacobson and S. Whitelam, Direct evaluation of dynamical large-deviation rate functions using a variational ansatz, *Phys. Rev. E* **100**, 052139 (2019).
- [11] T. Nemoto, R. L. Jack, and V. Lecomte, Finite-size scaling of a first-order dynamical phase transition: Adaptive population dynamics and an effective model, *Phys. Rev. Lett.* **118**, 115702 (2017).
- [12] U. Ray, G. K.-L. Chan, and D. T. Limmer, Exact fluctuations of nonequilibrium steady states from approximate auxiliary dynamics, *Phys. Rev. Lett.* **120**, 210602 (2018).
- [13] M. C. Bañuls and J. P. Garrahan, Using matrix product states to study the dynamical large deviations of kinetically constrained models, *Phys. Rev. Lett.* **123**, 200601 (2019).
- [14] S. Whitelam, D. Jacobson, and I. Tamblyn, Evolutionary reinforcement learning of dynamical large deviations, *J. Chem. Phys.* **153**, 044113 (2020).
- [15] C. Casert, T. Vieijra, S. Whitelam, and I. Tamblyn, Dynamical large deviations of two-dimensional kinetically constrained models using a neural-network state ansatz, *Phys. Rev. Lett.* **127**, 120602 (2021).
- [16] L. Causer, I. Lesanovsky, M. C. Bañuls, and J. P. Garrahan, Dynamics and large deviation transitions of the xor-fredrickson-andersen kinetically constrained model, *Phys. Rev. E* **102**, 052132 (2020).
- [17] P. Helms and G. K.-L. Chan, Dynamical phase transitions in a 2d classical nonequilibrium model via 2d tensor networks, *Phys. Rev. Lett.* **125**, 140601 (2020).
- [18] L. Causer, M. C. Bañuls, and J. P. Garrahan, Optimal sampling of dynamical large deviations via matrix product states, *Phys. Rev. E* **103**, 062144 (2021).
- [19] H. Touchette, The large deviation approach to statistical mechanics, *Phys. Rep.* **478**, 1 (2009).
- [20] R. L. Jack, Ergodicity and large deviations in physical systems with stochastic dynamics, *Eur. Phys. J. B* **93**, 1 (2020).
- [21] H. Ge and H. Qian, Analytical mechanics in stochastic dynamics: Most probable path, large-deviation rate function and hamilton–jacobi equation, *Int. J. Mod. Phys. B* **26**, 1230012 (2012).
- [22] Z. Lu and H. Qian, Emergence and breaking of duality symmetry in generalized fundamental thermodynamic relations, *Phys. Rev. Lett.* **128**, 150603 (2022).
- [23] U. Seifert, Stochastic thermodynamics, fluctuation theorems and molecular machines, *Rep. Prog. Phys.* **75**, 126001 (2012).
- [24] Y. Tang, R. Yuan, J. Chen, and P. Ao, Work relations connecting nonequilibrium steady states without detailed balance, *Phys. Rev. E* **91**, 042108 (2015).
- [25] C. Kwon, J. D. Noh, and H. Park, Nonequilibrium fluctuations for linear diffusion dynamics, *Phys. Rev. E* **83**, 061145 (2011).
- [26] Y. Tang, Free energy amplification by magnetic flux for driven quantum systems, *Commun. Phys.* **4**, 1 (2021).
- [27] K. Mallick, H. Moriya, and T. Sasamoto, Exact solution of the macroscopic fluctuation theory for the symmetric exclusion process, *Phys. Rev. Lett.* **129**, 040601 (2022).
- [28] P. Mehta, M. Bukov, C.-H. Wang, A. G. Day, C. Richardson, C. K. Fisher, and D. J. Schwab, A high-bias, low-variance introduction to machine learning for physicists, *Phys. Rep.* (2019).
- [29] G. Carleo, I. Cirac, K. Cranmer, L. Daudet, M. Schuld, N. Tishby, L. Vogt-Maranto, and L. Zdeborová, Machine learning and the physical sciences, *Rev. Mod. Phys.* **91**, 045002 (2019).
- [30] D. Wu, L. Wang, and P. Zhang, Solving statistical mechanics using variational autoregressive networks, *Phys. Rev. Lett.* **122**, 080602 (2019).
- [31] J.-G. Liu, L. Mao, P. Zhang, and L. Wang, Solving quantum statistical mechanics with variational autoregressive networks and quantum circuits, *Mach. Learn. Sci. Technol.* **2**, 025011 (2021).
- [32] G. Carleo and M. Troyer, Solving the quantum many-body problem with artificial neural networks, *Science* **355**, 602 (2017).
- [33] Z.-Y. Han, J. Wang, H. Fan, L. Wang, and P. Zhang, Unsupervised generative modeling using matrix product states, *Phys. Rev. X* **8**, 031012 (2018).
- [34] M. J. Hartmann and G. Carleo, Neural-network approach to dissipative quantum many-body dynamics, *Phys. Rev. Lett.* **122**, 250502 (2019).

[35] F. Vicentini, A. Biella, N. Regnault, and C. Ciuti, Variational neural-network ansatz for steady states in open quantum systems, *Phys. Rev. Lett.* **122**, 250503 (2019).

[36] A. Nagy and V. Savona, Variational quantum monte carlo method with a neural-network ansatz for open quantum systems, *Phys. Rev. Lett.* **122**, 250501 (2019).

[37] N. Yoshioka and R. Hamazaki, Constructing neural stationary states for open quantum many-body systems, *Phys. Rev. B* **99**, 214306 (2019).

[38] T. Westerhout, N. Astrakhantsev, K. S. Tikhonov, M. I. Katsnelson, and A. A. Bagrov, Generalization properties of neural network approximations to frustrated magnet ground states, *Nat. Commun.* **11**, 1593 (2020).

[39] A. Bohrdt, S. Kim, A. Lukin, M. Rispoli, R. Schittko, M. Knap, M. Greiner, and J. Léonard, Analyzing nonequilibrium quantum states through snapshots with artificial neural networks, *Phys. Rev. Lett.* **127**, 150504 (2021).

[40] G. H. Fredrickson and H. C. Andersen, Kinetic ising model of the glass transition, *Phys. Rev. Lett.* **53**, 1244 (1984).

[41] J. Jäckle and S. Eisinger, A hierarchically constrained kinetic ising model, *Z. für Phys. B* **84**, 115 (1991).

[42] L. Causer, M. C. Bañuls, and J. P. Garrahan, Finite time large deviations via matrix product states, *Phys. Rev. Lett.* **128**, 090605 (2022).

[43] C. W. Gardiner, *Handbook of Stochastic Methods*, 3rd ed. (Springer-Verlag, Berlin, 2004).

[44] J. P. Garrahan, R. L. Jack, V. Lecomte, E. Pitard, K. van Duijvendijk, and F. van Wijland, First-order dynamical phase transition in models of glasses: an approach based on ensembles of histories, *J. Phys. A* **42**, 075007 (2009).

[45] C. Maes, Frenesy: Time-symmetric dynamical activity in nonequilibria, *Phys. Rep.* **850**, 1 (2020).

[46] S. Pressé, K. Ghosh, J. Lee, and K. A. Dill, Principles of maximum entropy and maximum caliber in statistical physics, *Rev. Mod. Phys.* **85**, 1115 (2013).

[47] M. Suzuki, Generalized trotter's formula and systematic approximants of exponential operators and inner derivations with applications to many-body problems, *Commun. Math. Phys.* **51**, 183 (1976).

[48] R. J. Williams, Simple statistical gradient-following algorithms for connectionist reinforcement learning, *Machine Learning* **8**, 229 (1992).

[49] See Supplemental Material at [URL will be inserted by publisher] for details on the framework, the VAN, training of neural networks, the importance sampling and additional results of the dynamical partition function and the phase transition.

[50] A. Van Oord, N. Kalchbrenner, and K. Kavukcuoglu, Pixel recurrent neural networks, in *International conference on machine learning* (PMLR, 2016) pp. 1747–1756.

[51] J. Gu, Z. Wang, J. Kuen, L. Ma, A. Shahroudy, B. Shuai, T. Liu, X. Wang, G. Wang, J. Cai, *et al.*, Recent advances in convolutional neural networks, *Pattern Recognit.* **77**, 354 (2018).

[52] Z. Wu, S. Pan, F. Chen, G. Long, C. Zhang, and P. S. Yu, A comprehensive survey on graph neural networks, *IEEE Trans. Neural Netw. Learn Syst.* **32**, 4 (2021).

[53] F. Scarselli, M. Gori, A. C. Tsoi, M. Hagenbuchner, and G. Monfardini, The graph neural network model, *IEEE Trans. Neural Netw.* **20**, 61 (2008).

[54] R. L. Jack, I. R. Thompson, and P. Sollich, Hyperuniformity and phase separation in biased ensembles of trajectories for diffusive systems, *Phys. Rev. Lett.* **114**, 060601 (2015).

[55] L. Causer, J. P. Garrahan, and A. Lamacraft, Slow dynamics and large deviations in classical stochastic fredkin chains, [arXiv:2202.06989](https://arxiv.org/abs/2202.06989) (2022).

[56] I. Biazzo, A. Braunstein, L. Dall'Asta, and F. Mazza, Epidemic inference through generative neural networks, [arXiv:2111.03383](https://arxiv.org/abs/2111.03383) (2021).

[57] S. Falkner, A. Coretti, S. Romano, P. Geissler, and C. Dellago, Conditioning normalizing flows for rare event sampling, [arXiv:2207.14530](https://arxiv.org/abs/2207.14530) (2022).

[58] M. Reh, M. Schmitt, and M. Gärttner, Time-dependent variational principle for open quantum systems with artificial neural networks, *Phys. Rev. Lett.* **127**, 230501 (2021).

[59] M. Reh and M. Gärttner, Variational monte carlo approach to partial differential equations with neural networks, [arXiv:2206.01927](https://arxiv.org/abs/2206.01927) (2022).

[60] D. Luo, Z. Chen, J. Carrasquilla, and B. K. Clark, Autoregressive neural network for simulating open quantum systems via a probabilistic formulation, *Phys. Rev. Lett.* **128**, 090501 (2022).

[61] K. A. Nicoli, S. Nakajima, N. Strodthoff, W. Samek, K.-R. Müller, and P. Kessel, Asymptotically unbiased estimation of physical observables with neural samplers, *Phys. Rev. E* **101**, 023304 (2020).

[62] M. Hibat-Allah, M. Ganahl, L. E. Hayward, R. G. Melko, and J. Carrasquilla, Recurrent neural network wave functions, *Phys. Rev. Research* **2**, 023358 (2020).

[63] M. Germain, K. Gregor, I. Murray, and H. Larochelle, Made: Masked autoencoder for distribution estimation, [arXiv:1502.03509](https://arxiv.org/abs/1502.03509) (2015).

[64] K. Cho, B. Van Merriënboer, D. Bahdanau, and Y. Bengio, On the properties of neural machine translation: Encoder-decoder approaches, [arXiv:1409.1259](https://arxiv.org/abs/1409.1259) (2014).

[65] A. Van den Oord, N. Kalchbrenner, L. Espeholt, O. Vinyals, A. Graves, *et al.*, Conditional image generation with pixelcnn decoders, *Advances in neural information processing systems* **29** (2016).

[66] D. P. Kingma and J. Ba, Adam: A method for stochastic optimization, [arXiv:1412.6980](https://arxiv.org/abs/1412.6980) (2014).

[67] G. M. Rotskoff, A. R. Mitchell, and E. Vanden-Eijnden, Active importance sampling for variational objectives dominated by rare events: Consequences for optimization and generalization, [arXiv:2008.06334](https://arxiv.org/abs/2008.06334) (2021).

[68] J. Yan, H. Touchette, and G. M. Rotskoff, Learning nonequilibrium control forces to characterize dynamical phase transitions, *Phys. Rev. E* **105**, 024115 (2022).

[69] R. L. Jack and P. Sollich, Large deviations of the dynamical activity in the east model: analysing structure in biased trajectories, *J. Phys. A* **47**, 015003 (2013).

Supplemental Material to “Solving nonequilibrium statistical mechanics by evolving autoregressive neural networks”

In the Supplemental Material, we demonstrate the algorithm of learning the dynamical partition function by tracking the time evolution of the probability distribution over time. We also provide the setting of the variational autoregressive network (VAN) and details of the training and examples. The mathematical derivation of the Supplemental Material is in a self-consistent manner.

A reinforcement-learning approach to train autoregressive neural networks

To track the time evolution under the tilted generator \mathbb{W}_s for a small time point $\delta t = t_{i+1} - t_i \ll 1$, we use the Suzuki-Trotter decomposition [47]. Given the probability distribution $\hat{P}_i^{\theta_i}(\mathbf{x}, s)$ (the hat symbol denotes that the probability is expressed by the neural network model) at the current time point i and the tilted generator $e^{\delta t \mathbb{W}_s}$ with the counting field s (the strength of tilting), we estimate the next-step probability vector $|\hat{Q}_i^{\theta_i}\rangle = e^{\delta t \mathbb{W}_s} |\hat{P}_i^{\theta_i}\rangle / Z_{i+1}(s)$ with the normalization constant $Z_{i+1}(s)$. We learn the evolved distribution with a variational ansatz $\hat{P}_{i+1}^{\theta_{i+1}}(\mathbf{x}, s)$ by minimizing the loss function of its distance to the evolved distribution. We consider the Kullback-Leibler (KL)-divergence at each time point i :

$$\begin{aligned} D_{KL}[\hat{P}_{i+1}^{\theta_{i+1}} || \hat{Q}_i^{\theta_i}] &= \sum_{\mathbf{x}} \hat{P}_{i+1}^{\theta_{i+1}}(\mathbf{x}, s) [\ln \hat{P}_{i+1}^{\theta_{i+1}}(\mathbf{x}, s) - \ln \hat{Q}_i^{\theta_i}(\mathbf{x}, s)] \\ &= \sum_{\mathbf{x}} \hat{P}_{i+1}^{\theta_{i+1}}(\mathbf{x}, s) [\ln \hat{P}_{i+1}^{\theta_{i+1}}(\mathbf{x}, s) - \ln e^{\delta t \mathbb{W}_s} \hat{P}_i^{\theta_i}(\mathbf{x}, s)] + \ln Z_{i+1}(s), \end{aligned} \quad (9)$$

where D_{KL} denotes the KL-divergence and the summation $\sum_{\mathbf{x}}$ is over all the possible configurations.

The probability distributions $\hat{P}_{i+1}^{\theta_{i+1}}(\mathbf{x}, s), \hat{P}_i^{\theta_i}(\mathbf{x}, s)$, with the parameters denoted by θ , can be parameterized by the VAN. Under the tilted dynamical operator, the probability vector acted on by the operator $e^{\delta t \mathbb{W}_s} |\hat{P}_i^{\theta_i}\rangle$ is not conserved, i.e., the normalization constant $Z_{i+1}(s)$ is unknown in advance and needs to be estimated. However, the VAN represents an automatically normalized model by design [30], and thus the distribution $\hat{P}_{i+1}^{\theta_{i+1}}(\mathbf{x}, s)$ is renormalized after each iteration. With the renormalization, we can draw samples from the normalized distribution $\hat{P}_{i+1}^{\theta_{i+1}}(\mathbf{x}, s)$ to evaluate the expectation $\mathbb{E}_{\mathbf{x} \sim \hat{P}_{i+1}^{\theta_{i+1}}}[\dots]$.

The loss function at each time step is defined as the KL-divergence without the normalization constant:

$$\begin{aligned} \mathcal{L}_{i+1} &= \sum_{\mathbf{x}} \hat{P}_{i+1}^{\theta_{i+1}}(\mathbf{x}, s) [\ln \hat{P}_{i+1}^{\theta_{i+1}}(\mathbf{x}, s) - \ln \mathbb{T}_s \hat{P}_i^{\theta_i}(\mathbf{x}, s)] \\ &= \mathbb{E}_{\mathbf{x} \sim \hat{P}_{i+1}^{\theta_{i+1}}} [\ln \hat{P}_{i+1}^{\theta_{i+1}}(\mathbf{x}, s) - \ln \mathbb{T}_s \hat{P}_i^{\theta_i}(\mathbf{x}, s)], \end{aligned} \quad (10)$$

where the transition operator $\mathbb{T}_s = (\mathbb{I} + \delta t \mathbb{W}_s) \approx e^{\delta t \mathbb{W}_s}$. In the expectation, \mathbf{x} are samples drawn from the distribution $\hat{P}_{i+1}^{\theta_{i+1}}(\mathbf{x}, s)$: $\mathbb{E}_{\mathbf{x} \sim \hat{P}_{i+1}^{\theta_{i+1}}}[\dots] \approx \sum_{\mathbf{x}} \hat{P}_{i+1}^{\theta_{i+1}}(\mathbf{x}, s)[\dots]$. In the main text, we use the notation $\sum_{\mathbf{x}} \hat{P}_{i+1}^{\theta_{i+1}}(\mathbf{x}, s)[\dots]$ for the summation of the samples generated from the distribution.

Due to the nonnegativity of the KL-divergence in Eq. (9) we have:

$$\mathcal{L}_{i+1} \geq -\ln Z_{i+1}(s), \quad (11)$$

where the equality holds when the VAN accurately learns the evolved probability distribution. Then, the minimized loss leads to the normalization constant at each time step, with more details provided below.

The operator \mathbb{W}_s can be specified for each model. For kinetically constrained models (KCMs), where the state transition occurs for states with only one-spin difference, we only need to evaluate N (the number of spin sites) manipulations to have all the transitions into or out from each sampled state for $\mathbb{T}_s \hat{P}_i^{\theta_i}(\mathbf{x}, s)$. This procedure can be executed in parallel for all the samples in the batch.

The parameters θ_{i+1} can be updated by minimizing the loss function [30]:

$$\begin{aligned}
\nabla_{\theta_{i+1}} \mathcal{L}_{i+1} &= \nabla_{\theta_{i+1}} \sum_{\mathbf{x}} \hat{P}_{i+1}^{\theta_{i+1}}(\mathbf{x}, s) [\ln \hat{P}_{i+1}^{\theta_{i+1}}(\mathbf{x}, s) - \ln \mathbb{T}_s \hat{P}_i^{\theta_i}(\mathbf{x}, s)] \\
&= \sum_{\mathbf{x}} \{ [\nabla_{\theta_{i+1}} \hat{P}_{i+1}^{\theta_{i+1}}(\mathbf{x}, s)] \cdot [\ln \hat{P}_{i+1}^{\theta_{i+1}}(\mathbf{x}, s) - \ln \mathbb{T}_s \hat{P}_i^{\theta_i}(\mathbf{x}, s)] + \hat{P}_{i+1}^{\theta_{i+1}}(\mathbf{x}, s) \nabla_{\theta_{i+1}} \ln \hat{P}_{i+1}^{\theta_{i+1}}(\mathbf{x}, s) \} \\
&= \mathbb{E}_{\mathbf{x} \sim \hat{P}_{i+1}^{\theta_{i+1}}} \{ [\nabla_{\theta_{i+1}} \ln \hat{P}_{i+1}^{\theta_{i+1}}(\mathbf{x}, s)] \cdot [\ln \hat{P}_{i+1}^{\theta_{i+1}}(\mathbf{x}, s) - \ln \mathbb{T}_s \hat{P}_i^{\theta_i}(\mathbf{x}, s)] \},
\end{aligned} \tag{12}$$

where we have used the log-derivative technique $\nabla_{\theta} P_{\theta} = P_{\theta} \cdot \nabla_{\theta} \ln P_{\theta}$ and used the fact that $\mathbb{E}_{\mathbf{x} \sim \hat{P}_{i+1}^{\theta_{i+1}}} [\nabla_{\theta_{i+1}} \ln \hat{P}_{i+1}^{\theta_{i+1}}(\mathbf{x}, s)] = \nabla_{\theta_{i+1}} \sum_{\mathbf{x}} \hat{P}_{i+1}^{\theta_{i+1}}(\mathbf{x}, s) = \nabla_{\theta_{i+1}} 1 = 0$ when the number of samples is sufficient. This gradient estimator is called REINFORCE [48] in the machine learning community.

The variance reduction is included to reduce the variance of the loss function [30].

As a different way of updating the parameters, a time-dependent variational method was developed in [58, 59] and can be used for training the neural network. However, inverting the Fisher-metric matrix may be computationally demanding when the number of neural-network parameters increases.

Evaluating the dynamical partition function

Although the VAN was applied to evolve quantum systems [58, 60], there is a lack of a framework to track the unnormalized probability evolution under tilted dynamics, which is necessary to uncover the dynamical phase transition. Here, with the learnt VAN, we can evaluate the dynamical partition function under the tilted operator. When learning VAN at each time step, the normalization factor as the volume change of the distribution has the information of the partition function. We record the normalization factor at each time step and multiply all of them to obtain the dynamical partition function.

Specifically, the dynamical partition function is obtained by applying e^{tW_s} to the steady state:

$$Z_t(s) = \langle -|e^{tW_s}|ss \rangle, \tag{13}$$

where $|ss\rangle$ is the steady state vector and $\langle -|$ is the flat state as the left eigenvector of the generator. For the system with detailed balance, the Hermitian form of the operator can be used by a similarity transformation $W_s \rightarrow \mathbb{P}^{-1/2} W_s \mathbb{P}^{1/2}$, where $\mathbb{P}^{-1/2}$ is a diagonal matrix of the steady-state probability [44].

Evaluating $Z_t(s)$ by Eq. (13) requires full matrix manipulation. Alternatively, we can obtain the normalization constant by using samples from the learnt VAN as follows. By the Suzuki-Trotter decomposition [47], the partition function Eq. (13) can be evaluated sequentially:

$$\begin{aligned}
Z_t(s) &\approx \langle -|[e^{\delta t W_s}]^I|ss \rangle \\
&= \langle -|[e^{\delta t W_s}]^{I-1} e^{\delta t W_s}|ss \rangle \\
&\approx \langle -|[e^{\delta t W_s}]^{I-1} |\hat{P}_1^{\theta_1}(s)\rangle Z_1(s), \\
&\approx \dots \\
&\approx \langle -|\hat{P}_I^{\theta_I}(s)\rangle \prod_{i=1}^I Z_i(s) \\
&= \prod_{i=1}^I Z_i(s),
\end{aligned} \tag{14}$$

where the probability vector at each time step, such as $|\hat{P}_1^{\theta_1}(s)\rangle$, is learned by the VAN as a normalized distribution. The first approximation has an error incurred by the Suzuki-Trotter decomposition, and the remaining approximations have the error resulting from training the VAN. The last step is due to the normalization property of the VAN.

The normalization constants $Z_i(s)$ can be estimated by the variational free energy $\mathcal{F}_i^{\theta_i}(s)$ when the VAN learns the distribution. That is,

$$\ln Z_t(s) \approx \sum_{i=1}^I \ln Z_i(s) = - \sum_{i=1}^I \mathcal{F}_i(s) \geq - \sum_{i=1}^I \mathcal{F}_i^{\theta_i}(s), \tag{15}$$

where the equality in the last step holds when the VAN accurately learns the evolved distribution at each time step. Since we do not have the energy function (Hamiltonian) from the model, it is infeasible to calculate the normalization constant by Eq. (S12) in [30]. Note that the distribution $\hat{P}_i^{\theta_i}$ yielded by the VAN cannot be directly used to calculate the partition function either because the VAN is already normalized.

Here, the variational free energy at the time step $i + 1$ is estimated from the loss function Eq. (10) at the end of training:

$$\mathcal{F}_{i+1}^{\theta_{i+1}}(s) = \mathcal{L}_{i+1}. \quad (16)$$

To better approximate the summation on all the configurations in Eq. (10) for calculating \mathcal{L}_{i+1} , one may also consider reweighting the expectation [61] of calculating the variational free energy. For example, $\mathbb{E}_{\mathbf{x} \sim \hat{P}_{i+1}^{\theta_{i+1}}}[\dots] = \sum_{\mathbf{x} \sim \hat{P}_{i+1}^{\theta_{i+1}}} \{\hat{P}_{i+1}^{\theta_{i+1}}(\mathbf{x}, s) \cdot [\dots]\} / [\sum_{\mathbf{x}' \sim \hat{P}_{i+1}^{\theta_{i+1}}} \hat{P}_{i+1}^{\theta_{i+1}}(\mathbf{x}', s)]\}$, and the summations are on all the drawn samples. This reweighting is the same as the importance sampling, Eq. (9) in [61], which can help the accuracy of the sampled average. We find this reweighting procedure useful in examples.

The moments of the dynamical observable are obtained by taking derivatives of the dynamical partition function. For example, the average dynamical activity per unit time and site follows from the partition function:

$$k_t(s) = -\frac{1}{Nt} \frac{d}{ds} \ln Z_t(s). \quad (17)$$

Higher moments can be estimated similarly.

With the above, the pseudocode of our method is summarized in ALGORITHM 1.

Input: The system size and dimension, the model type, the boundary condition, time steps, values of the counting field s .
Output: The evolved probability distributions over time by the VAN, normalization factors at each time step, and the dynamical partition function.

Choose an initial distribution, such as the steady state of the non-tilted dynamics.

for Every time step **do**

Learn the next-step VAN $\hat{P}_{i+1}^{\theta_{i+1}}(\mathbf{x}, s)$:

for Every epoch **do**

1. Draw samples $\{\mathbf{x}\}$ from the VAN;

2. Calculate relevant matrix elements of the transition operator \mathbb{T}_s to get $\mathbb{T}_s \hat{P}_i^{\theta_i}(\mathbf{x}, s)$;

3. Train the VAN by minimizing the loss function: $\mathcal{L}_{i+1} = \mathbb{E}_{\mathbf{x} \sim \hat{P}_{i+1}^{\theta_{i+1}}} [\ln \hat{P}_{i+1}^{\theta_{i+1}}(\mathbf{x}, s) - \ln \mathbb{T}_s \hat{P}_i^{\theta_i}(\mathbf{x}, s)]$.

end for

Calculate the variational free energy at each time step: $\mathcal{F}_{i+1}^{\theta_{i+1}}(s) = \mathcal{L}_{i+1}$ after training.

end for

Calculate the dynamical partition function: $Z_t(s) \approx \prod_{i=1}^t Z_i(s)$, $\ln Z_i(s) \approx \mathcal{F}_i^{\theta_i}(s)$.

ALGORITHM 1. Tracking time evolution of the probability distribution and dynamical partition function by the VAN.

The method of projection

In examples, we evolve the system for a sufficiently long time when the accumulation rate of the partition function converges. A longer simulation time leads to a state closer to the steady state.

We further provide a method to save the computational time of evolving the state. It employs the convergence of the dynamical partition function in the long-time limit to extrapolate from the finite time. In the long-time limit, Eq. (13) becomes $Z_t(s) \sim e^{t\theta(s)}$, where $\theta(s)$ is the scaled cumulant generating function (SCGF) [19]. One can use the variational Monte-Carlo to calculate the SCGF $\theta(s)$ in the long-time limit [15]: Note that the VAN there represents the wave function with its square being normalized, but here it represents the probability distribution.

Then, we rewrite the dynamical partition function as:

$$Z_t(s) = e^{t\theta(s)} \langle -|e^{t[\mathbb{W}_s - \theta(s)]}|ss \rangle. \quad (18)$$

The modified tilted generator is:

$$\hat{W}_s = \sum_{\mathbf{x}' \neq \mathbf{x}} e^{-s} w_{\mathbf{x}, \mathbf{x}'} |\mathbf{x}'\rangle \langle \mathbf{x}| - [r_{\mathbf{x}} + \theta(s)] |\mathbf{x}\rangle \langle \mathbf{x}|. \quad (19)$$

In the long-time limit, the logarithmic dynamical partition function eventually converges to a linear function of time with the slope θ , and all but the leading eigenvector are exponentially damped. Therefore, the slope of $\ln \langle -|e^{t[\hat{W}_s - \theta(s)]} |ss\rangle$ should converge to nearly zero, at which the simulation can be stopped to extrapolate the long-time limit by using the SCGF. Around the phase transition, the time scale of the convergence may diverge.

Although the operator \hat{W}_s has the zero largest eigenvalue, it is not a stochastic operator. Indeed, the operator \hat{W}_s is different from the Doob operator [18], which can be annihilated by the left flat state.

Variational autoregressive networks

We use the variational autoregressive network [30, 31] to parameterize the probability distribution. The VAN factorizes the joint probability into a product of conditional probabilities as:

$$\hat{P}^{\theta}(\mathbf{x}) = \prod_{i=1}^N \hat{P}^{\theta}(x_i | x_1, \dots, x_{i-1}), \quad (20)$$

where x_i denotes the d_s -dimensional variable of site i , and θ represents the learnable parameters. The parameterized distribution is automatically normalized, which is also called autoregressive modeling in the machine learning community. Since each conditional probability only depends on previous sites, it supports efficient *ancestral sampling* in parallel.

For the kinetically constrained models, we used RNN [62] for 1D and 2D, PixelCNN [50] for 2D, and MADE [63] for 3D. In 1D, we found RNN to be more accurate than MADE. In 2D, RNN had a comparable accuracy with PixelCNN but took a longer computational time. Below, we briefly describe the architecture of the RNN and gated PixelCNN for our problem. The setting of MADE was the same as [30].

Recurrent neural networks

For the recurrent neural network (RNN), we use a gated recurrent unit (GRU) [64] as the recurrent cell, which is capable of learning the distribution with long-range correlations. It is more efficient than the long-short time memory (LSTM) model and avoids the vanishing gradient problem for vanilla recurrent neural networks.

For the 1D RNN, the conditional probability is iteratively obtained over the one-dimensional sites. A recurrent cell processes the information from the previous hidden state h_{i-1} and the input data x_{i-1} in the current cell, generates a new hidden state h_i , gives the conditional probability $\hat{P}^{\theta}(x_i | x_1, \dots, x_{i-1})$ based on h_i , and passes on the information of h_i to the next cell. The dimension of the hidden states is denoted by d_h . The GRU has a candidate hidden state \hat{h}_i , an update gate z_i interpolating between the previous and candidate hidden states, and a reset gate r_i setting the extent of forgetting for the previous hidden state. It updates by the following gates:

$$z_i = \sigma(W_{zx}x_{i-1} + W_{zh}h_{i-1} + b_z), \quad (21)$$

$$r_i = \sigma(W_{rx}x_{i-1} + W_{rh}h_{i-1} + b_r), \quad (22)$$

$$\hat{h}_i = \tanh(W_{hx}x_{i-1} + W_{hh}(r_i \odot h_{i-1}) + b_h), \quad (23)$$

$$h_i = (1 - z_i) \odot h_{i-1} + z_i \odot \hat{h}_i, \quad (24)$$

where W s are the weight matrices, b s are bias vectors, and σ is the sigmoid activation function, \odot denotes the Hadamard product.

The conditional probability is obtained from the hidden states. The output is acted on by a linear transform and a softmax operator $\hat{P}^{\theta}(x_i | x_1, \dots, x_{i-1}) = \text{Softmax}(W h_i + b)$, which ensures the normalized condition for the output probability vector. Given an initial hidden state h_0 and variable \mathbf{x}_0 (chosen as a zero vector here), the full probability is obtained by Eq. (20) with the iteratively generated conditional probabilities. Sampling from the probability distribution is conducted similarly: given an initial hidden state and variable, the variable x_1 is sampled from the estimated conditional probability, and the procedure is repeated to the last site.

For the 2D RNN, the implementation is more involved. A zigzag path [15, 62] is used to transmit the lattice variables, both vertical and horizontally. For the vertical and horizontal variables (hidden state h and variable x separately), we first concentrate the two into one and perform a linear transform (without the bias term) to an intermediate variable with the original dimension. They are then passed to the next GRU cell to continue the iteration.

The gated PixelCNN

For 2D lattice systems, we find that the vanilla PixelCNN model [50] suffers from the blind spot problem. In the worst case, the blind spot in the receptive field only covers half of the sites above and to the left of the current site. To circumvent the blind spot problem, we use the gated PixelCNN [65] that combines two convolutional network stacks: the vertical stack and the horizontal stack. The vertical stack conditions on all the sites left and the horizontal stack conditions on all the sites above. The activation function is also replaced by a gated activation unit:

$$\mathbf{h}^{i+1} = \tanh(W_1^i * \mathbf{h}^i) \odot \sigma(W_2^i * \mathbf{h}^i) \quad (25)$$

where i is the number of layers, \mathbf{h}^i is the feature map at the i -th layer and \odot denotes the stacked convolution operation.

Details of training neural networks

For KCMs, the time step length is often chosen as $dt = 0.05$, and the range $dt \in [0.01, 0.1]$ is typically suitable. The loss usually takes $> \mathcal{O}(10^3)$ epochs to converge for the first time step of evolving the system but requires only $\mathcal{O}(10^2)$ epochs for the following time steps because the probability distribution only has a small change after each time step. The less required epoch after the first time step saves the training time for tracking the evolution.

Learning rates affect the accuracy of training. Among the tested learning rates 10^{-5} , 10^{-4} , 10^{-3} , and 10^{-2} , we found that 10^{-3} typically leads to relatively lower loss values and better training. It is possible to encounter general optimization issues such as trapping into local minima, which may be alleviated by designing schedulers for the learning rate.

We used the Adam optimizer [66] to perform the stochastic gradient descent. The batch size was usually set as 1000 for each epoch. To better estimate the variational free energy, we used the batch from the last 20% of the training epochs, where the loss converges. This average gives a more accurate estimate by using approximately $1000 \times 100 \times 20\%$ (batch size, total epoch at each time point, last percent of the training epochs) batch samples.

The accuracy of the VAN depends on the number of depths and widths of the neural network. We used 8, 16, 32, 64, 128 as the number of hidden states in RNN and found that 64, 128 generally gives lower loss for one-layer RNN. A larger number of hidden states and more hidden layers require a longer computational time.

We list the number of depths and widths of the neural network with the best performance in our attempts for each model (Fig. 3). The table also provides the corresponding computational time on various systems sizes and dimensions under a single core GPU ($\sim 25\%$ usage) of Tesla-V100.

Furthermore, we generated configurations with symmetry of the lattice systems, e.g., the parity symmetry for 1D spin systems and the rotational plus reflectional symmetry for 2D cases. The imposed symmetry does not significantly improve the accuracy of the training or the estimation on the dynamical partition function, with a cost of more computational time. Therefore, symmetry was not included in most of our numerical implementations but was added as an option in our code package for specific tasks that require the imposing of symmetry.

The relative error

We estimated the error of the VAN under each dimension. To quantify the accuracy of the VAN, we calculated the relative error of the dynamical partition functions between the VAN and the numerically exact result. The numerically exact result of the dynamical partition function was obtained by summing up probabilities of all possible states, which is feasible only for systems with small sizes, e.g., approximately $L \leq 10$ for 1D, $L \leq 4$ for 2D, and $L \leq 2$ for 3D. For larger system sizes, the numerically exact result was not accessible which then demands the use of the present algorithm.

The relative error e_r is defined as:

$$e_r = \left| \frac{\ln Z_t(s) - \ln Z_t(s)_{\text{exact}}}{\ln Z_t(s)_{\text{exact}}} \right|. \quad (26)$$

Type	Finite time: 10^2 epoch for one time step							
Dimension	1			2			3	
Time steps	10^4			$4 * 10^3$			$4 * 10^3$	
Lattice size L	10, +	20	40	4, +	5	6	2, +	3
VAN type	RNN	RNN	RNN	Gated PixelCNN/ RNN	Gated PixelCNN/ RNN	Gated PixelCNN/ RNN	MADE	MADE
VAN size (depth, width)	1,128	1,128	1,128	3,32/1,128	3,32/1,128	3,32/1,128	4,16	4,16
Total computational time for one s value by 1/4 Tesla-V100 (hour)	16.83	11.37	65.28	4.09/16.63	8.01/32.12	12.24/56.43	2.68	5.74

FIG. 3. (Color online) The table for the chosen VAN size and the computational time for a certain number of time steps. The systems under 1D, 2D, 3D, and with different lattice lengths are considered. The lattice size with * means that the computational time includes that of calculating the numerically exact result. The learning rate is 10^{-3} with the Adam optimizer [66]. The batch size is 1000, and the time step is $dt = 0.05$.

The error is shown in the inset of Fig. 4a for 1D and Fig. 6 for 2D and 3D. All the figures show that the relative error is usually smaller than $\mathcal{O}(10^{-3})$ compared with the numerically exact result, validating the accuracy of the VAN.

Based on the accuracy and the efficiency, we chose the more appropriate VAN for each dimension: the RNN in 1D, the gated PixelCNN in 2D, and the MADE in 3D.

Methods of improving the accuracy of the VAN

The accuracy of VAN is especially demanding near the phase transition because rare configurations at different phases need to be sampled to train the VAN. To improve the efficiency, we provide two methods to help sample rare configurations: importance sampling and proper initialization for the VAN. These strategies may be employed near the phase transition of KCMs.

Importance sampling

For KCMs, the active phase has many spin flips, so the number of up spins should not be small. There are many such configurations for the active phase. For the inactive phase, spins do not flip often, and the number of up spins must be small, which are rare configurations. These rare configurations are hard to sample, leading to the inefficiency of training the VAN from the active to the inactive phase.

To sample rare configurations more effectively, we leverage importance sampling. We first employ a distribution where rare configurations have higher probability. We sample from this distribution and perform probability reweighting when calculating the expected value over the VAN distribution:

$$\mathbb{E}_{\mathbf{x} \sim \hat{P}^\theta} \{ \dots \} = \mathbb{E}_{\mathbf{x} \sim \tilde{P}} \{ (\hat{P}^\theta / \tilde{P}) \dots \} = \mathbb{E}_{\mathbf{x} \sim \tilde{P}} \{ \exp(\ln \hat{P}^\theta - \ln \tilde{P}) \dots \}, \quad (27)$$

\hat{P}^θ is the distribution by the VAN, and \tilde{P} is a prior distribution.

For KCMs, we use the binomial distribution as \tilde{P} with $p = 1/N$, where N is the total number of spins, such that the average up spin from the distribution is 1. Therefore, configurations with only one up spin can be sampled out frequently. In general, importance sampling needs to be designed for the specific problem, with the distribution \tilde{P} tailored to sample particular configurations. After adding the samples from the importance samples, the learning rate may be decreased to reduce the loss variance.

With this strategy, the estimation on the SCGF at the steady state and the finite-time evolution becomes more accurate for all values of the counting field s . The detailed setting of the importance sampling may differ between these two tasks. For calculating the SCGF, adding approximately fifty samples from the important sampling to the one thousand batch ($\sim 5\%$) from the VAN improved the efficiency of estimating the SCGF.

To track the finite-time evolution, we added a few samples, e.g., one sample, from the important sampling to the batch with a thousand samples from the VAN. This accelerated the search of the inactive phases of KCMs. The proper number of added samples is dependent on the system size and specific problems and may need to be fine-tuned to control the system in certain phases. Under the same number of samples from the importance sampling, the PixelCNN was more robust under various s , that is, the inactive and active phases were both efficiently learnt. The RNN with importance sampling was more sensitive to the counting field s .

The active importance sampling for neural networks was proposed in [67], where umbrella sampling and replica exchange were used. However, it is not directly applicable in the present setting because the normalization constant of the windowing functions in Eq. (18) is not computable for the current case. Instead, here, we employed a normalized prior distribution, compatible with the rare configurations of KCMs. In addition, the present importance sampling is on the configurations from a distribution at each time point, different from the importance sampling on trajectories, which may be harder to sample.

Proper choices on the initialization of the VAN

To accurately estimate the SCGF at the steady state with $s > 0$, we conducted the variational Monte Carlo simulation [15] to calculate the SCGF, both from small to large s and from large to small s . When going from small to large, we used the VAN trained under small s as the initial VAN for the next larger one, and vice versa when going from large to small. This estimation employed the VAN either from the active phase with smaller s or the inactive phase with larger s thus enabling us to find the more proper phases for the current s . Then, we took the larger value of the SCGF from the two results, serving as the best estimation on the SCGF.

For finite time, one may save the VAN at each time point and various s . Then, it is useful to employ information from different s by using the VAN under the neighbor values of chosen s to calculate the evolved distribution. This helps to improve the efficiency of sampling rare configurations at different phases, which may generate a more accurate estimation of the dependence of the dynamical phase transition on s . This strategy shares a similar spirit of the replica exchange in [68], where two trajectories corresponding to different s are swapped. Here, configurations at each time point rather than trajectories were shared between different s .

To capture the time point where phase transition occurs, we can also employ the method of choosing a good candidate of the VAN as the initial model for the training at each time point. To better capture a phase transition, two initialized VANs may be used: one from the previous time point, and the other from the steady-state variational Monte-Carlo calculation. After training, the one with lower loss is chosen, such that the model closer to the optimal solution is found at any time point.

Based on the above two strategies of importance sampling and proper VAN initialization, we have a protocol for uncovering the full phase diagram of dynamical observables for a given nonequilibrium system. Taking the active-inactive phase transition of the KCM as an example, one can first calculate the SCGF at the steady state by using the variational Monte-Carlo method, with the importance sampling or a proper initialization of the VAN, such that the active-inactive phase transition versus the counting field can be precisely revealed. Second, the present method tracks the time evolution of the dynamical observable. If there is a mismatch between the long-time dynamical observable and that from the SCGF, such as around the phase transition point, one may turn on the importance sampling at a certain time point to better capture the active-inactive phase transition over time.

Kinetically constrained models

One-dimensional cases

For 1D models, we chose the boundary sites with up spins [42]. The results are plotted in Fig. 4 with positive s and Fig. 5 with negative s . They show consistent behaviors with previous results [13, 42, 69], validating our approach for one-dimensional systems.

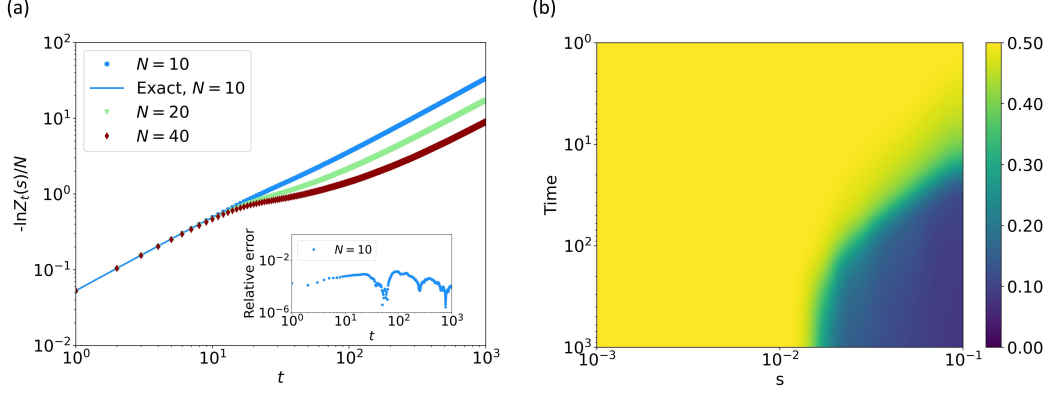


FIG. 4. (Color online) The dynamical partition function and phase transition for the 1D FA model. (a) The logarithmic dynamical partition function $\ln Z_t(s)$ over time ($c = 0.5, s = 0.1, N = 10, 20, 40$). $N = 10$ is compared with the numerically exact result by storing the full probability distribution. The time step is chosen as $dt = 0.1$, and the plotted time points are taken from every 10 steps to better visualize the comparison with the numerically exact result for $N = 10$. (b) The dynamical activity $k_t(s)$ denoted by the color reveals the dynamical phase transition over time for the 1D FA with $N = 20$ and $c = 0.5$.

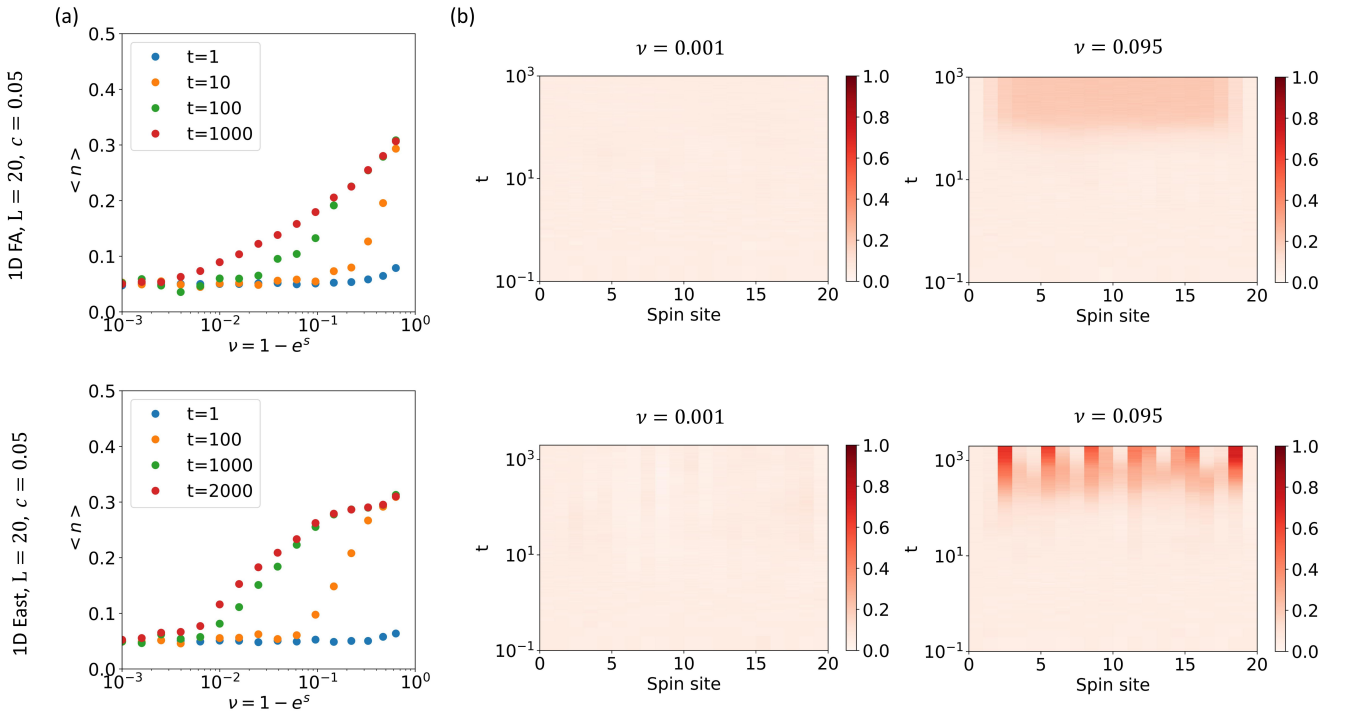


FIG. 5. (Color online) Emergence of active phases for 1D models. The 1D FA (top) and East (bottom) models with $c = 0.05$ and negative s . (a) The average up spins for different negative s versus $\nu = 1 - e^s$ at several time points. (b) For $c = 0.05$, the East model forms structures with up spins separated by down spins. The FA model does not have such structures but more up spins over time at the middle of the 1D chain. The color denotes the average number of up spins. These behaviors are consistent with the previous result by the tensor network [42].

Two-dimensional cases

For the 2D and 3D models, we set the boundary sites with down spins. The dynamical phase transition is accurately tracked (Fig. 6), with the error shown in the inset. Since the computational time required is high for tracking the time evolution, the chosen lattice size L is $L = 4$ for the quantum system [30]. Here, we need to further estimate the time evolution under various values of the counting field s and thus considered $L = 4, 5, 6$ in 2D and $L = 2, 3, 4$ in 3D.

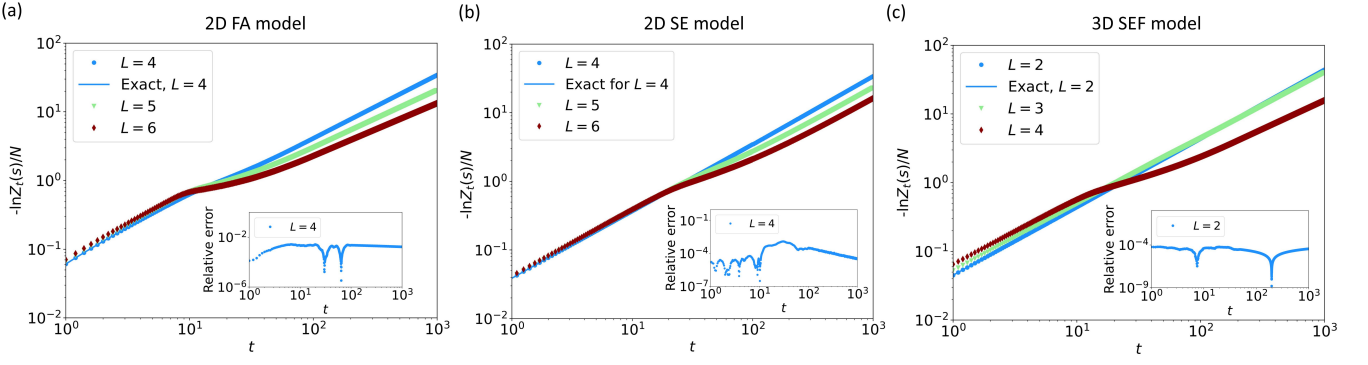


FIG. 6. (Color online) Time evolution of the dynamical partition function for the 2D FA, 2D SE and 3D SEF models. (a) The logarithmic dynamical partition function $\ln Z_t(s)$ over time in a $L \times L$ lattice ($c = 0.5, s = 0.1, L = 4, 5, 6$). The tilt of the curve indicates the dynamical phase transition (see text). $L = 4$ is compared with the numerically exact solution by storing the full probability distribution, and the relative error is plotted in the inset. (b) The same as (a) for the 2D SE model with $c = 0.5, s = 0.1, L = 4, 5, 6$. (c) The same as (a) for the 3D SEF model with $c = 0.5, s = 0.1, L = 2, 3, 4$.

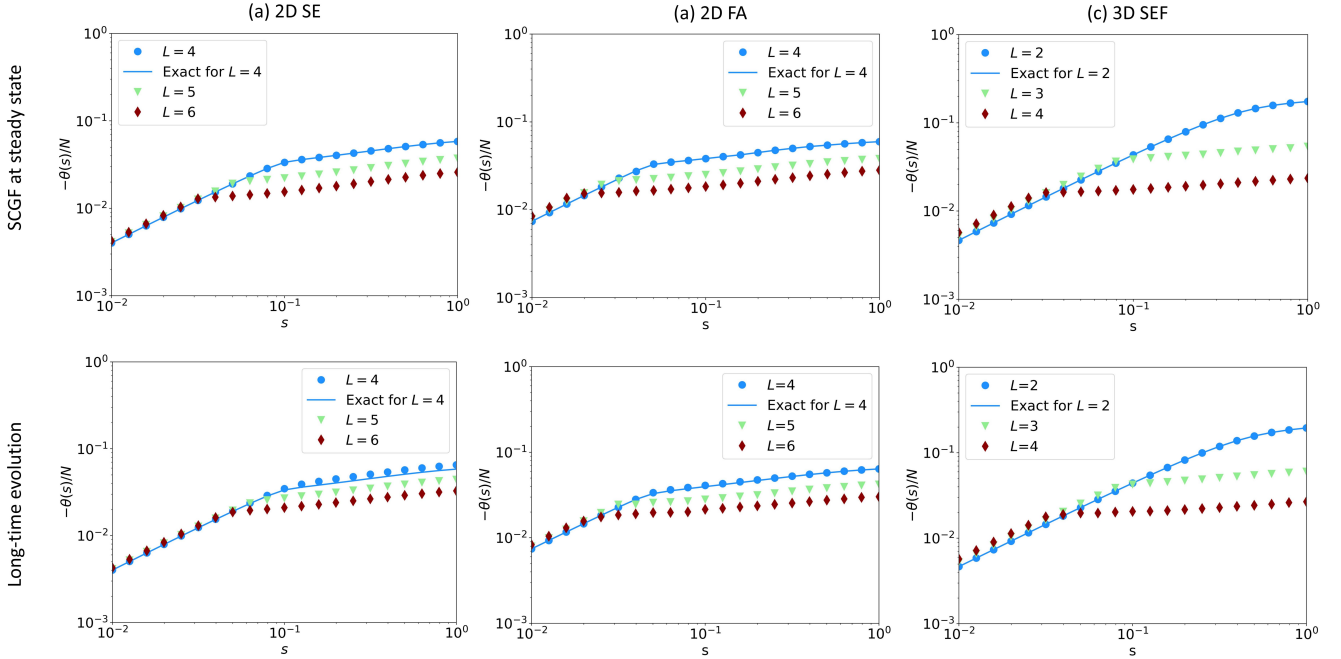


FIG. 7. (Color online) The consistency between the long-time evolution and SCGF at steady state for (a) the 2D SE, (b) the 2D FA, and (c) the 3D SEF models. (Top) The SCGF at the steady state calculated from the variational Monte Carlo method. (Bottom) The logarithm of the dynamical partition function at the last time point, which agrees with the top panel. For the smallest lattice size in each panel, the present method matches well with the numerically exact result.

For $s > 0$ in 2D, we used values of the counting field logarithmically, i.e., $\log_{10} s \in [-2, 0]$ with the interval 0.1. With the result under discrete values of s , we used the interpolation and smoothed the phase transition line, which does not affect the physical result on the phase transition, such as its scaling on time. The present finite-time result at the last time point also converges to the SCGF at steady state (Fig. 7), calculated from the variational Monte-Carlo method [15]. The remaining deviation comes from the fact that the last time point may have not fully reached the steady state and the error from the Suzuki-Trotter decomposition.

Since all the boundary sites have down spins, the configuration with all down spins is an absorbing configuration. Thus, it should be excluded from the system evolution because otherwise it will absorb the probabilities of all other configurations. For the 2D SE model, the first spin is fixed up to overcome this issue. For the 2D FA model, we used the setting without fixing the first spin up and excluded the disconnected configuration with all down spins,

consistent with the setting in [15]. Specifically, in the last spin site, we manually chose it to be up if every previous site has down spins by setting the probability of the last up spin to be 1, such that the configuration with all down spins has probability zero. This setting also ensures the normalization condition of the total probabilities.

For $s < 0$ in 2D, the values of the counting field were also chosen logarithmically, i.e., $\log_{10}(-s) \in [-3, 0]$ with the interval 0.2. We use $\nu = 1 - e^s$ as the horizontal axis in Fig. 2. Here, we have fixed the left-up spin up for both the 2D FA and 2D SE models to better compare their characteristic spatial structures. Using more samples increases the accuracy of estimating the average density, and a longer simulation time may be required to reach closer to the steady state.

Three-dimensional cases

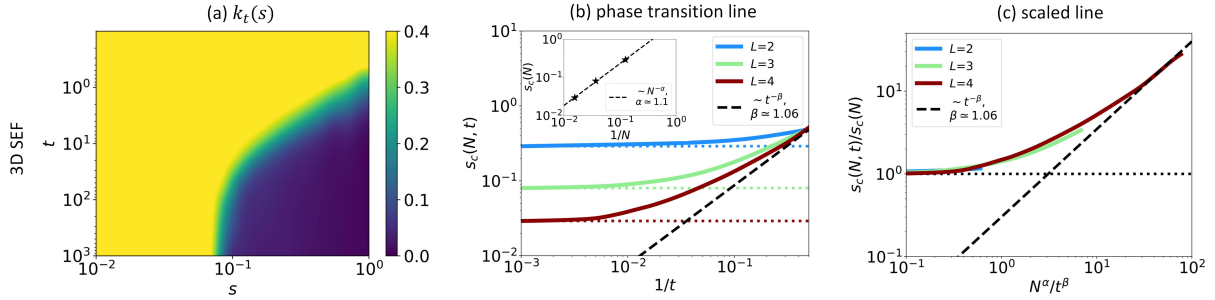


FIG. 8. (Color online) The dynamical phase transition over time for the 3D SEF model. (a) The dynamical activity $k_t(s)$ over time t versus the counting field s , with $L = 3$. The color denotes the dynamical activity. (b) The critical point $s_c(N, t)$ over time, giving critical exponents α for $s_c(N) \sim N^{-\alpha}$ at the steady state and β for $t^{-\beta}$. (c) The scaled phase transition lines are collapsed together, with $s_c(N, t)/s_c(N)$ and time scaled as $N^\alpha t^{-\beta}$. Parameters: $c = 0.5$, $L = 2, 3, 4$ for 3D.

We consider the South-East-Front (SEF) model in 3D as a natural extension of the South-East model in 2D. The SEF model in 3D has f_i count the number of up spins only for the left, above, and back nearest neighbors. To implement the VAN, we used a three-dimensional version of MADE [63] by first translating the three-dimensional lattice into a one-dimensional chain.

We applied the method to track the dynamical phase transition of the 3D SEF model with $L = 2, 3, 4$ (Fig. 8). The critical exponent of size $\alpha \gtrsim 1$, which is similar to the 1D [13] and 2D [15] cases. The critical exponent of time $\beta \approx 1$ is similar to the 1D case in [42] and the 2D case obtained in the present work. The results of the 2D and 3D models demonstrate that our approach is able to track the finite-time evolution of the probability distribution for higher dimensional cases.